Published in final edited form as:
Biomaterials. 2008 May ; 29(13): 2015–2024. doi:10.1016/j.biomaterials.2007.12.049.

Non-invasive characterization of structure and morphology of silk fibroin biomaterials using non-linear microscopy

William L. Rice[1], **Shamaraz Firdous**[2], **Sharad Gupta**[1], **Martin Hunter**[1], **Cheryl Wong Po Foo**[1], **Yongzhong Wang**[1], **Hyeon Joo Kim**[1], **David L. Kaplan**[1], and **Irene Georgakoudi**[1,*]

[1] Biomedical Engineering Department, Tufts University, 4 Colby Str, Rm. 153, Medford, Massachusetts 02155, USA

[2] Laser Lab, Department of Physics & Applied Mathematics (DPAM), Pakistan Institute of Engineering & Applied Sciences (PIEAS), P. O. Nilore, Islamabad, Pakistan

Abstract

Designing biomaterial scaffolds remains a major challenge in tissue engineering. Key to this challenge is improved understanding of the relationships between the scaffold properties and its degradation kinetics, as well as the cell interactions and the promotion of new matrix deposition. Here we present the use of non-linear spectroscopic imaging as a non-invasive method to characterize not only morphological, but also structural aspects of silkworm silk fibroin-based biomaterials, relying entirely on endogenous optical contrast. We demonstrate that two photon excited fluorescence and second harmonic generation are sensitive to the hydration, overall β sheet content and molecular orientation of the sample. Thus, the functional content and high resolution afforded by these non-invasive approaches offer promise for identifying important connections between biomaterial design and functional engineered tissue development. The strategies described also have broader implications for understanding and tracking the remodeling of degradable biomaterials under dynamic conditions both *in vitro* and *in vivo*.

Keywords

Silk; Fibroin; Non-linear Microscopy; Two-photon excited fluorescence; Second Harmonic Generation; Spectral Analysis; Non-invasive characterization

1. Introduction

Design optimization of the biomaterials that are used as scaffolds onto which new or regenerated tissues are expected to grow is one of the major challenges facing tissue engineers. Numerous aspects of the biomaterials design, from the molecular structure and organization to the overall macro-architecture of these systems are known to impact significantly the development of new tissue *in vitro* and *in vivo*[1–4]. Scaffolds provide structural support and important environmental cues to cells that populate them, thus controlling to a large extent

*Correspondence should be addressed to IG. E-mail: Irene.Georgakoudi@tufts.edu Fax: 617-627-3231.

Competing interest statement
The authors declare that they have no competing financial interest.

cellular proliferation[1,5], differentiation[6–8], deposition of new structural proteins[9,10] and ultimately the regeneration of functional tissue[4,11,12]. Traditionally, methods such as NMR, FTIR and X-Ray spectroscopy have been used to assess biomaterials at the molecular level [13–17], while SEM and TEM have been invaluable tools for characterizing the three dimensional morphology of biomaterial scaffolds [5,18–23]. Histology and immunostaining as well as assays for determining the expression levels of specific proteins are often used to assess how scaffolds interact with cells as tissues develop[5,10,18,20,22–24]. While all of these approaches provide sensitive and specific data, they are invasive. As a result, they reveal information about a single time-point along the development of a dynamically changing specimen. This limitation hinders full characterization and understanding of the relationships that exist between the structural, mechanical, architectural and biochemical properties of the scaffold and the corresponding properties of the developing tissue.

A number of optical methods have been developed to monitor non-invasively different tissue components in the context of disease diagnosis and monitoring[25–29]. Such methods have only recently started to be exploited as tools for assessing different properties of the cell and matrix components of engineered tissues[30–33]. The goal of this study was to determine the type of morphological and structural information that could be acquired about silk-based biomaterial scaffolds using spectral two-photon excited fluorescence (TPEF) and second harmonic generation (SHG) imaging. This information will be essential in developing an optical biomarker toolkit that will allow us to monitor dynamically how such scaffolds interact with and are modified by cells as engineered tissues grow either *in vitro* or *in vivo*. Furthermore, these optical toolkits can also be extended to other biomaterial matrices as the systems are developed and optimized.

Silk is a natural protein polymer valued for its biocompatibility, light weight, and strength [34] Processing methods for this polymer are well established for control of morphology, mechanical properties and environmental stability [35–38]. Due to these properties, silk is an excellent candidate for generating biomaterial scaffolds for engineered tissues. The *Bombyx mori* silkworm silk protein, fibroin, can be described by two structural models: Silk I, consisting of type II β turn, random coil domains, and mixed structures including alpha helices, and Silk II, consisting mostly of antiparallel β pleated sheets. [14,15]. The β sheet content and the alignment of these β sheet crystals, along with the non-crystalline domains of the protein, are important determinants of the bulk mechanical properties and degradation kinetics of biomaterials generated from silk[14,36,37,39–41]. Most of theβ sheet content and orientation of these crystalline domains is lost during the processing of silk fibroin into aqueous solutions, a step required for the regeneration of new biomaterial scaffolds for tissue culture[42]. The β sheet content and orientation can be reconstituted to different extents depending on the mode of material preparation[14,38,42]. Thus, the non-invasive, optical assessment of β sheet content and orientation of silk fibroin during biomaterial scaffold formation was one of the specific goals of this study.

Linear optical approaches, such as fluorescence and Raman spectroscopy have been used previously to characterize materials made from silk fibroin[39,43,44]. However, there are no studies to our knowledge on the nonlinear optical properties of silk. Nonlinear optical methods such as TPEF and SHG offer additional advantages for non-invasive imaging including excitation in the near infrared region of the spectrum, where scattering is typically lower than in the visible region, and reduced photobleaching[45]. In TPEF and SHG two photons, typically of the same energy, interact simultaneously with a molecule and yield either fluorescence emission (TPEF) or scattering (SHG) of a single photon. In the case of SHG, the scattered photon has the same energy as the collective energy of the two incident photons (i.e. there is no net energy loss and the wavelength of the scattered photon is at exactly half the wavelength of each one of the incident photons). In the case of TPEF, the wavelength of the incident photons

is approximately twice as long as the wavelength of a photon required for linear excitation, while the fluorescently emitted photons have nearly identical spectral features as those resulting from single photon excitation. Because the probability of simultaneous interaction with two photons is orders of magnitude lower than single photon interactions, TPEF and SHG processes require the presence of high photon densities. As a result, these events are confined within a small volume in the apex of a focused cone of light and automatically yield optically sectioned, depth-resolved images. The confinement of the optical effect, and the use of low energy (longer wavelength) photons results in reduced thermal and photo damage within and outside the plane of focus [45]. Exploiting such processes in microscopic imaging platforms allows frequent sample assessment over long periods of time, without damage or contamination from elements outside the tissue culture environment.

2. Materials and Methods

All chemicals were obtained from Sigma Aldrich (St. Louis, MO) unless otherwise noted.

2.1. Preparation of silk fibroin

Cocoons of *B. mori* were kindly provided by M. Tsukada (Institute of Sericulture, Tsukuba, Japan). The cocoons were initially processed to remove the glue-like sericin proteins and to extract the pure silk fibroin component as previously described [39]. The resulting aqueous silk fibroin solution had an approximate concentration of 8% (wt) silk fibroin. For hexafluoro-2-propanol (HFIP) silk fibroin solutions, aqueous silk was lyophilized and redissolved in HFIP resulting in a 6% (w/v) fibroin solution.

2.2. Preparation of films and gels

Silk fibroin films were made by pipetting volumes of aqueous or HFIP silk solutions onto 35mm glass bottom dishes (MatTek, Acton MA) and allowing the solvent to evaporate. Gels were made from aqueous solutions in 35mm glass bottom dishes at silk concentrations of 8% and 4% with 6% (vol) 0.1M HCl. The silk solutions were placed on the dishes first and the acid was titrated into the solution for a final volume of 2.5 mL.

Dishes were then sealed with paraffin film and placed at 37°C for 72 hours [42]. β sheet content was induced in silk fibroin films by immersion in methanol for 30 minutes. Films were compressed and stretched by placing films in opposing clamps, applying pressure to secure the film and then drawing the clamps apart.

2.3. Preparation of scaffolds

Three dimensional silk scaffolds were prepared as previously described [39]. The scaffolds were cut into discs (5 mm in diameter and 3 mm in thickness) dried at 60° C, and autoclaved for further experiments. The pore size of the scaffolds was 550±30 μm.

Human mesenchymal stem cells (Cambrex, East Rutherford NJ) were seeded onto an aqueous silk scaffold as described by Kim et al[19]. The seeded scaffolds were placed on glass bottom dishes and imaged on day 21.

2.4. Two-photon Excited Fluorescence and Second Harmonic Generation Microscopy

TPEF and SHG micrographs were acquired on a Leica DMIRE2 microscope with a TCS SP2 scanner (Wetzlar, Germany). The system was equipped with a 10× (NA 0.3) dry, 20× (NA 0.7) dry and a 63× (NA 1.2) water immersion objective. The excitation light source was a Mai Tai tunable (710–920nm) titanium sapphire laser emitting 100 fs pulses at 80MHz (Spectra Physics, Mountain View CA). Samples were placed on culture dishes with number 1.5 cover glass bottoms (MATTEK, Ashland MA) and excited at 800 nm. Fluorescence emission spectra

were detected from 380 nm to 700 nm in 30 steps with a 20 nm detector bandwidth. Fluorescence images were acquired simultaneously by two non-descanned PMTs with a filter cube containing a 700 nm short pass filter (Chroma SPC700bp) a dichroic mirror (Chroma 495dcxr), and emitter bandpass filters centered at 455 nm (Chroma 455bp70) and 525 nm (Chroma 525bp50). SHG images were acquired in the forward direction through a bandpass filter centered at 400 nm (Chroma hq400/20m-2p). Analysis was performed with the Leica Confocal Software (Wetzlar, Germany) and Matlab (Mathworks, Natick MA).

2.5. FTIR Analysis

FTIR spectroscopy was performed on a Bruker Equinox 55 FTIR spectrometer (Billerica, MA, USA). Measurements were made over 64 scans with a resolution of 4 cm^{-1} over the range of 400 – 4000 cm^{-1}. Data were collected with the Opus 4 software.

2.6. Polarized Raman Spectroscopy

Raman polarized spectra were recorded at room temperature and in the backscattering configuration using a Hololab 5000R Raman spectrometer (Kaiser Optical Systems, Inc., Ann Arbor, MI) coupled to a microscope. The samples were studied using the 785 nm line of a near infra red solid state laser (Kaiser, Invictus 785), which was focused using a 50X objective (0.75 NA) and provided an excitation power at the sample of approximately 5 mW. Spectra were collected using a holographic grating and a CCD detector. The fluorescence background was removed using a polynomial function.

3. Results and Discussion

3.1. Assessment of β sheet content in silk fibroin biomaterials through TPEF emission spectra

To assess the detailed TPEF features of silk, we acquired spectral images in the 380 to 700 nm range from silk fibroin generated at different processing stages and in different biomaterial formats. Specifically, we examined silk in aqueous solution, dried aqueous and hexafluoroisopropanol (HFIP)-processed films, films with β sheet content induced by methanol treatment, hydrogels induced by pH changes, aqueous and HFIP-processed scaffolds, and natural silk fibers. We demonstrate in Figure 1 that TPEF spectra excited at 800 nm are sensitive to the secondary structure of the silk fibroin protein, and more specifically its β sheet content and hydration status. The dependence of the silk TPEF spectral emission on β sheet content is demonstrated in panel A, through repeated measurements of an aqueous 8% silk solution, whose secondary structure is changing dynamically over a period of 22 hours as it transforms into a hydrogel, in response to the addition of 6% by volume 0.1N HCl. In particular, a progressive blue shift occurs in the emission spectra of the fibroin, as the β sheet content increases during the formation of the hydrogel[42]. The ability to monitor and characterize such changes in the same sample in a manner that doesn't interfere at all with the specimen is one of the main advantages of TPEF spectral imaging approaches. A schematic representation of the structural changes that are probably occurring in the hydrogel that lead to the observed spectral shifts is included in Fig. 1B. Note that these schematics do not attempt to provide an accurate representation of silk structure. The increase in β sheet content was confirmed by the presence of a dominant FTIR peak at 1625 cm^{-1}(Fig. 1E) [14]. This peak is absent from the FTIR spectrum of a dried aqueous solution (aqueous film, Fig. 1E), which exhibits a strong peak at 1650 cm^{-1}, characteristic of random coil and α helical protein structures present in the silk I conformation. We have also observed an enhancement in the blue region of the spectrum of silk fibroin films upon methanol treatment, as shown in the inset of Fig. 1A for an HFIP-treated film. Similar TPEF spectra have been acquired from aqueous films. The induction of β sheet formation upon methanol treatment was confirmed by FTIR studies (Fig. 1E). A blue shift is also present when comparing the spectra of aqueous silk solutions and hydrated silk

scaffolds or aqueous silk films and dry scaffolds (Fig. 1C), further supporting our conclusion that spectral shape can be correlated to β sheet content of silk fibroin samples.

In processed biomaterials, β sheets are formed by increasing hydrophobic interactions, which generate crystalline domains. These domains are insoluble in water and contribute to the environmental stability and mechanical properties of the protein-based material, acting as physical crosslinks[35,37,46,47]. Thus, the ability to assess β sheet content non-invasively by TPEF spectroscopy could serve as an important quality control or monitoring tool for assessing the conformation and the dynamic changes in silk protein structures prior to and following cell interactions and implantation for tissue engineering applications. Tracking changes in this feature would also provide a direct window into degradation profiles during scaffold and tissue regeneration *in vitro* or *in vivo*.

3.2. Assessment of hydration in silk fibroin biomaterials through TPEF emission spectra

Further examination of the TPEF spectral features reveals that emission is sensitive not only to the β sheet content of the sample, but also to the environment surrounding the silk fibroin. Specifically, as shown in Figure 1C, we observe a blue shift in the emission spectra that correlates with a decrease in hydration, which is expected to have an impact primarily on the noncrystalline regions of the silk protein. For example, drying of the aqueous solution results in a film with a blue shifted emission spectrum (Fig. 1C). The fibroin in both the film and the solution is in random coil and α helix conformations, as confirmed by FTIR studies (Figure 1E). Similarly, a dry silk scaffold has a blue shifted TPEF spectrum compared to that of a hydrated silk scaffold (Figure 1C). A TPEF spectrum from natural silk fibers is also included in Fig. 1C and it exhibits very similar features to those of a dry silk scaffold.

Spectral shifts in response to a more polar environment have been observed for chromophores such as tryptophan, and are typically attributed to changes in the relaxation of the molecule because of polar interactions or the formation of hydrogen bound complexes in the excited state[48–50]. We expect that similar processes are responsible for the observed red shift in the silk spectra of samples exposed to more highly hydrated environments, depicted schematically in Fig. 1D.

Since enhanced hydration has been correlated with changes in viscoelastic properties in studies involving both silkworm [51] and spider silk [52], the observed spectral shifts may be used to non-invasively assess features associated with the expected mechanical behavior of silk-based tissue engineered constructs. This would include dynamic changes *in vitro* and *in vivo* during matrix remodeling.

3.3. Characterization of silk fibroin biomaterial morphology through TPEF and SHG images

Acquisition of TPEF spectral information is essential for characterizing and understanding the shifts that are reported in Figure 1. However, based on the spectral details of fibroin fluorescence emission, it is possible to identify a small number of wavelength regions that are sensitive to the observed dependencies on silk II content and hydration. The appropriate choice of emission filters to cover these spectral windows provides for a simpler, more efficient method of monitoring changes in the fluorescence properties of silk biomaterials. The histogram in Figure 1F represents such an approach, based on calculation of the ratio of the average fluorescence intensity from images collected through two optical filters covering the 410–485 nm and 500–550 nm regions. The aqueous silk solution, with the most red-shifted emission spectrum has the lowest fluorescence ratio, while dry silk scaffolds and natural fibers have the highest ratio (Figure 1F). The gradual blue shift observed in the emission spectrum from aqueous solution, to film (aqueous and HFIP-treated) and film with β sheet content is reflected in the progressive increase of the fluorescence ratio as well (Figure 1F). The red shift

of the emission spectrum due to hydration of the silk scaffold corresponds to a decrease of the fluorescence ratio from dry to hydrated scaffold (Figure 1F). Finally, the fluorescence ratio from hydrogels lies between hydrated and dry silk scaffolds indicating a balance between the contributions from β sheets and the affects of hydration on the TPEF emission. This also indicates a current limitation of the technique to isolate the spectral effects of hydration and β sheet composition, i.e. if both properties are changing at the same time it would not be possible for TPEF to separate their contributions to the corresponding spectral shifts.

TPEF images (red) were acquired from the different silk samples at these two spectral emission bands along with corresponding SHG images (green) (Fig. 2). Only the TPEF images acquired in the 500–550 nm window are included in Figure 2, since the morphological features revealed by the images in the 410–485 nm region are nearly identical. We find that individual natural silk fibres, containing highly oriented secondary structures (Figure 2C) possess strong TPEF and SHG signals and can be easily distinguished (Fig. 2A and 2B). The fibers are processed into aqueous solutions from which films, hydrogels and scaffolds are made. Fibroin films cast from this solution are uniformly fluorescent, but they do not produce SHG (Fig. 2D and 2E). Representative images are shown from an aqueous, β sheet containing (i.e. methanol-treated) film, whose main structural features are depicted schematically in Figure 2F; a similar uniform morphology is also detected from non-methanol treated aqueous and HFIP-processed silk films (data not shown). Addition of HCl to the aqueous solutions alters the pH and results in the induction of β sheets and the formation of hydrogels that are fluorescent and exhibit no SHG (Fig. 2J – 2L). The heterogeneous distribution of the protein resulting from the addition of 6% HCl to a 4% silk solution can be seen in the fluorescence image. Scaffolds processed from the aqueous solution are strongly fluorescent and, in contrast to the film and gel samples, they exhibit SHG signal that is typically localized along pore edges (Fig. 2M and 2N). The gross morphology, pore size and surface roughness of the aqueous scaffold are easily discerned in the fluorescent image.

Morphological characterization of biomaterial features such as surface roughness are important with respect to material and tissue mechanical properties, cell interactions, tissue regeneration and remodeling *in vivo* and *in vitro*. [18,38,38,39,53]. This information is made readily available via three-dimensional reconstructions of TPEF-based optical sections, as shown in Figure 3 and 4. For example, significant differences in the morphology of aqueous and HFIP-treated silk scaffolds are seen in Fig. 3A and 3C, consistent with SEM observations (Fig. 3B and 3D). Very distinct architectures have also been observed in silk hydrogels created from different relative concentrations of silk and HCl (Fig. 3E and 3G). The highly uniform and the fibrillar morphologies achieved with the 8% silk, 6% HCl and 4% silk, 6% HCl, respectively, are confirmed by SEM (Fig. 3F and 3H). The level of architectural and morphological detail in all cases resembles closely that of SEM images acquired to assess features that are relevant in the 1–1000μm regime. Additionally these reconstructions of TPEF optical sections can be used to non invasively assess pore size and interconnections in true three dimensional fashion as depicted in the images of 3D models of aqueous scaffold sections (Figure 4 and corresponding animations). The image stack acquired with the 10X objective includes information from depths that are nearly 1 mm away from the surface, demonstrating the capability of the technique to assess architectural features over dimensions that are highly appropriate for tissue engineering applications.

The combined use of TPEF and SHG imaging not only provides a useful means of assessing morphological and structural features of silk scaffolds, but it also allows distinction of the silk features from those of other extracellular matrix proteins, such as collagen (Figure 5). Several studies have exploited SHG to visualize individual collagen fibers within engineered[54], *ex vivo* [26,55] and *in vivo* tissues[56]. A superposition of TPEF and SHG image stacks from a silk scaffold containing collagen fibers within its pores illustrates that it is possible to visualize

both components relying entirely on endogenous sources of optical contrast (Figure 5). This is possible because TPEF emission dominates the nonlinear optical response of silk, while collagen fibers yield strong SHG. Thus, non-invasive characterization and monitoring of the changes in scaffold content and structure in relationship to the deposited collagen matrix should be feasible during engineered tissue growth.

3.4 Structural origin of SHG from silk fibroin biomaterials

Of particular interest was the understanding of the origins of the SHG signal in the natural silk fibers and the silk scaffolds. SHG results from the asymmetric resonant scattering of two long wavelength light waves into a single higher energy wave and is observed from non centrosymmetric systems, such as collagen type I[26,57]. Natural silk fibers also yield a strong SHG signal, and we hypothesized that it originates from the highly oriented α-helical and β-sheet conformations, as depicted schematically in Figure 2C. As mentioned before, the secondary structure and alignment of the silk fibroin molecules is lost during solubilization. Depending on the subsequent processing into films, hydrogels and scaffolds, varying levels of the α-helical and β-sheet conformations are reconstituted, as assessed by FTIR, X-Ray scattering and Raman studies (Figure 1E and other studies [14,39,42,58]). To confirm that SHG requires the presence of aligned secondary structures, we acquired SHG images prior to and following compression and stretching of aqueous, methanol-treated silk films. A comparison of the detected images shown in Figures 2G–H reveals that this type of manipulation indeed leads to SHG. The intensity of the mean fluorescence of an image, and the shape of the emission spectrum did not change after stretching, indicating that a change in the amount of β sheet content was not responsible for the SHG.

To demonstrate that the presence of SHG is directly associated withβ sheet alignment, we performed polarized Raman micro-spectroscopy measurements of natural silk fibers and methanol treated silk films prior to and following compression/stretching. As shown in Figure 6, polarized Raman spectra acquired along the horizontal and vertical orientations relative to the fiber axis exhibit significant differences in the Raman peaks at 1665 and 1228 cm^{-1}, corresponding to the amide I and amide III modes, respectively. This is expected to occur as the C=O stretching (amide I) and the Alanine residue N-H in plane bending and CH_2 twisting (amide III) modes of aligned β sheets orient preferentially perpendicular to (amide I) and in parallel with (amide III) the fiber axis[39]. In contrast, the intensity of these peaks is almost identical for the methanol treated aqueous films, indicating the presence of randomly oriented β sheets. However, when the films are compressed and stretched, we detect a significant difference in the intensity of the 1228 cm^{-1} peak consistent with the induction of increased levels of aligned amide III N-H groups, and, thus, more highly oriented β sheets. Thus, these results support the notion that SHG is sensitive to the orientation of the β-sheets within silk fibroin. Therefore, the presence of SHG along the pores of silk scaffolds indicates the presence of such aligned secondary structures, as depicted in Figure 2O. It is likely that molecular orientation of the amorphous and α-helical domains of the protein also leads to an enhancement in SHG; however, more detailed studies are needed to assess these contributions. Mechanistically, we reported that salt-induced β sheet formation along the pores of the scaffold is responsible for the stabilization of these systems[38]; thus, overall β sheet alignment may still be low in the bulk material, while this localized region lining the pores may be in part responsible for the SHG.

4. Conclusion

In summary, the non-linear imaging and spectroscopy approaches outlined here could serve as important tools for assessing and monitoring silk-based and potentially other, biomaterial properties that may be particularly useful in the context of tissue engineering applications

(Table 1). Further studies could be performed to enhance the quantitative nature of these measurements and correlate, for example, specific spectral features to pre-determined levels of β-sheet content and hydration. The ability to non-invasively characterize key structural and architectural features of silk-based scaffolds based entirely on endogenous sources of optical contrast prior to and during tissue development should enhance significantly our understanding of the dynamic interactions between these biomaterial matrices and cells. More broadly, we expect that spectroscopic TPEF and SHG imaging will also be applicable to the dynamic characterization of other standard biomaterials, such as PGA, for example, which also exhibits strong non-linear fluorescence and scattering [59]. This, in turn, should allow for more efficient optimization in the design of biomaterials that promote development of functional tissues. Furthermore, the potential to use TPEF and SHG-based imaging not only *in vitro* but also *in vivo* makes these approaches particularly attractive as the field of tissue engineering evolves.

Supplementary Material

Refer to Web version on PubMed Central for supplementary material.

Acknowledgments

We thank Xiao Hu for help with FTIR measurements, and Brian Lawrence for his assistance with SEM. Funding for this work was provided by NSF (BES 0547292) and NIH (P41 EB002520). This work made use of MRSEC Shared Facilities supported by the National Science Foundation under Award Number DMR-0213282 and NSF Laser Facility grant #CHE-0111370.

References

1. Stevens MM, George JH. Exploring and engineering the cell surface interface. Science 2005;310:1135–1138. [PubMed: 16293749]
2. Behravesh E, Yasko AW, Engel PS, Mikos AG. Synthetic biodegradable polymers for orthopaedic applications. Clin Orthop Relat Res 1999;367(Suppl):S118–29. [PubMed: 10546641]
3. Agrawal CM, Ray RB. Biodegradable polymeric scaffolds for musculoskeletal tissue engineering. J Biomed Mater Res 2001;55:141–150. [PubMed: 11255165]
4. Hubbell JA. Biomaterials in tissue engineering. Biotechnology (N Y) 1995;13:565–576. [PubMed: 9634795]
5. Kim TG, Park TG. Biomimicking extracellular matrix: cell adhesive RGD peptide modified electrospun poly(D,L-lactic-co-glycolic acid) nanofiber mesh. Tissue Eng 2006;12:221–233. [PubMed: 16548681]
6. Mauney JR, Jaquiery C, Volloch V, Heberer M, Martin I, Kaplan DL. In vitro and in vivo evaluation of differentially demineralized cancellous bone scaffolds combined with human bone marrow stromal cells for tissue engineering. Biomaterials 2005;26:3173–3185. [PubMed: 15603812]
7. Mauney JR, Kirker-Head C, Abrahamson L, Gronowicz G, Volloch V, Kaplan DL. Matrix-mediated retention of in vitro osteogenic differentiation potential and in vivo bone-forming capacity by human adult bone marrow-derived mesenchymal stem cells during ex vivo expansion. J Biomed Mater Res A 2006;79:464–475. [PubMed: 16752403]
8. Kim BS, Mooney DJ. Development of biocompatible synthetic extracellular matrices for tissue engineering. Trends Biotechnol 1998;16:224–230. [PubMed: 9621462]
9. Griffith LG, Naughton G. Tissue engineering--current challenges and expanding opportunities. Science 2002;295:1009–1014. [PubMed: 11834815]
10. Edwards GA, Glattauer V, Nash TJ, White JF, Brock KA, Werkmeister JA, Ramshaw JA. In vivo evaluation of a collagenous membrane as an absorbable adhesion barrier. J Biomed Mater Res 1997;34:291–297. [PubMed: 9086398]
11. Griffith LG, Swartz MA. Capturing complex 3D tissue physiology in vitro. Nat Rev Mol Cell Biol 2006;7:211–224. [PubMed: 16496023]

12. Athanasiou KA, Niederauer GG, Agrawal CM. Sterilization, toxicity, biocompatibility and clinical applications of polylactic acid/polyglycolic acid copolymers. Biomaterials 1996;17:93–102. [PubMed: 8624401]
13. van Beek JD, Hess S, Vollrath F, Meier BH. The molecular structure of spider dragline silk: folding and orientation of the protein backbone. Proc Natl Acad Sci U S A 2002;99:10266–10271. [PubMed: 12149440]
14. Hu X, Kaplan D, Cebe P. Determining beta-sheet crystallinity in fibrous proteins by thermal analysis and infrared spectroscopy. Macromolecules 2006;39:6161–6170.
15. Asakura T, Ohgo K, Ishida T, Taddei P, Monti P, Kishore R. Possible implications of serine and tyrosine residues and intermolecular interactions on the appearance of silk I structure of Bombyx mori silk fibroin-derived synthetic peptides: high-resolution 13C cross-polarization/magic-angle spinning NMR study. Biomacromolecules 2005;6:468–474. [PubMed: 15638554]
16. Zhao C, Yao J, Masuda H, Kishore R, Asakura T. Structural characterization and artificial fiber formation of Bombyx mori silk fibroin in hexafluoro-iso-propanol solvent system. Biopolymers 2003;69:253–259. [PubMed: 12767126]
17. Simmons AH, Michal CA, Jelinski LW. Molecular orientation and two-component nature of the crystalline fraction of spider dragline silk. Science 1996;271:84–87. [PubMed: 8539605]
18. Kim HJ, Kim UJ, Vunjak-Novakovic G, Min BH, Kaplan DL. Influence of macroporous protein scaffolds on bone tissue engineering from bone marrow stem cells. Biomaterials 2005;26:4442–4452. [PubMed: 15701373]
19. Altman GH, Horan RL, Lu HH, Moreau J, Martin I, Richmond JC, Kaplan DL. Silk matrix for tissue engineered anterior cruciate ligaments. Biomaterials 2002;23:4131–4141. [PubMed: 12182315]
20. Brehmer B, Rohrmann D, Becker C, Rau G, Jakse G. Different types of scaffolds for reconstruction of the urinary tract by tissue engineering. Urol Int 2007;78:23–29. [PubMed: 17192728]
21. Xu CC, Chan RW, Tirunagari N. A Biodegradable, Acellular Xenogeneic Scaffold for Regeneration of the Vocal Fold Lamina Propria. Tissue Eng. 2006
22. Martin I, Shastri VP, Padera RF, Yang J, Mackay AJ, Langer R, Vunjak-Novakovic G, Freed LE. Selective differentiation of mammalian bone marrow stromal cells cultured on three-dimensional polymer foams. J Biomed Mater Res 2001;55:229–235. [PubMed: 11255174]
23. Xin X, Hussain M, Mao JJ. Continuing differentiation of human mesenchymal stem cells and induced chondrogenic and osteogenic lineages in electrospun PLGA nanofiber scaffold. Biomaterials 2007;28:316–325. [PubMed: 17010425]
24. Wang Y, Kim UJ, Blasioli DJ, Kim HJ, Kaplan DL. In vitro cartilage tissue engineering with 3D porous aqueous-derived silk scaffolds and mesenchymal stem cells. Biomaterials 2005;26:7082–7094. [PubMed: 15985292]
25. Gonzalez S, Swindells K, Rajadhyaksha M, Torres A. Changing paradigms in dermatology: confocal microscopy in clinical and surgical dermatology. Clin Dermatol 2003;21:359–369. [PubMed: 14678715]
26. Zipfel WR, Williams RM, Christie R, Nikitin AY, Hyman BT, Webb WW. Live tissue intrinsic emission microscopy using multiphoton-excited native fluorescence and second harmonic generation. Proc Natl Acad Sci U S A 2003;100:7075–7080. [PubMed: 12756303]
27. Ramanujam N. Fluorescence spectroscopy of neoplastic and non-neoplastic tissues. Neoplasia 2000;2:89–117. [PubMed: 10933071]
28. Fujimoto JG. Optical coherence tomography for ultrahigh resolution in vivo imaging. Nat Biotechnol 2003;21:1361–1367. [PubMed: 14595364]
29. Ntziachristos V, Chance B. Probing physiology and molecular function using optical imaging: applications to breast cancer. Breast Cancer Res 2001;3:41–46. [PubMed: 11250744]
30. Ko HJ, Tan W, Stack R, Boppart SA. Optical coherence elastography of engineered and developing tissue. Tissue Eng 2006;12:63–73. [PubMed: 16499443]
31. Tan W, Sendemir-Urkmez A, Fahrner LJ, Jamison R, Leckband D, Boppart SA. Structural and functional optical imaging of three-dimensional engineered tissue development. Tissue Eng 2004;10:1747–1756. [PubMed: 15684683]

32. Zoumi A, Yeh A, Tromberg BJ. Imaging cells and extracellular matrix in vivo by using second-harmonic generation and two-photon excited fluorescence. Proc Natl Acad Sci U S A 2002;99:11014–11019. [PubMed: 12177437]
33. Chandra M, Vishwanath K, Fichter GD, Liao E, Hollister SJ, Mycek MA. Quantitative molecular sensing in biological tissues: an approach to non-invasive optical characterization. Optics Express 2006;14:6157–6171. [PubMed: 19516787]
34. Shao Z, Vollrath F. Surprising strength of silkworm silk. Nature 2002;418:741. [PubMed: 12181556]
35. Altman GH, Diaz F, Jakuba C, Calabro T, Horan RL, Chen J, Lu H, Richmond J, Kaplan DL. Silk-based biomaterials. Biomaterials 2003;24:401–416. [PubMed: 12423595]
36. Jin HJ, Kaplan DL. Mechanism of silk processing in insects and spiders. Nature 2003;424:1057–1061. [PubMed: 12944968]
37. Liu Y, Shao Z, Vollrath F. Relationships between supercontraction and mechanical properties of spider silk. Nat Mater 2005;4:901–905. [PubMed: 16299506]
38. Kim UJ, Park J, Kim HJ, Wada M, Kaplan DL. Three-dimensional aqueous-derived biomaterial scaffolds from silk fibroin. Biomaterials 2005;26:2775–2785. [PubMed: 15585282]
39. Rousseau ME, Lefevre T, Beaulieu L, Asakura T, Pezolet M. Study of protein conformation and orientation in silkworm and spider silk fibers using Raman microspectroscopy. Biomacromolecules 2004;5:2247–2257. [PubMed: 15530039]
40. Jin HJ, Park J, Karageorgiou V, Kim UJ, Valluzzi R, Kaplan DL. Water-stable silk films with reduced beta-sheet content. Advanced Functional Materials 2005;15:1241–1247.
41. Kim UJ, Park J, Li C, Jin HJ, Valluzzi R, Kaplan DL. Structure and properties of silk hydrogels. Biomacromolecules 2004;5:786–792. [PubMed: 15132662]
42. Matsumoto A, Chen J, Collette AL, Kim UJ, Altman GH, Cebe P, Kaplan DL. Mechanisms of Silk Fibroin Sol-Gel Transitions. J Phys Chem B Condens Matter Mater Surf Interfaces Biophys 2006;110:21630–21638. [PubMed: 17064118]
43. Shao Z, Young RJ, Vollrath F. The effect of solvents on spider silk studied by mechanical testing and single-fibre Raman spectroscopy. Int J Biol Macromol 1999;24:295–300. [PubMed: 10342778]
44. Georgakoudi I, Tsai I, Greiner C, Wong C, DeFelice J, Kaplan D. Intrinsic fluorescence changes associated with the conformational state of silk fibroin in biomaterial matrices. Optics Express 2007;15:1043–1053. [PubMed: 19532332]
45. Zipfel WR, Williams RM, Webb WW. Nonlinear magic: multiphoton microscopy in the biosciences. Nat Biotechnol 2003;21:1369–1377. [PubMed: 14595365]
46. Bini E, Knight DP, Kaplan DL. Mapping domain structures in silks from insects and spiders related to protein assembly. J Mol Biol 2004;335:27–40. [PubMed: 14659737]
47. Huemmerich D, Slotta U, Scheibel T. Processing and modification of films made from recombinant spider silk proteins. Applied Physics A-Materials Science & Processing 2006;82:219–222.
48. Burstein EA, Abornev SM, Reshetnyak YK. Decomposition of protein tryptophan fluorescence spectra into log-normal components. I. Decomposition algorithms. Biophys J 2001;81:1699–1709. [PubMed: 11509382]
49. Reshetnyak YK, Burstein EA. Decomposition of protein tryptophan fluorescence spectra into log-normal components. II. The statistical proof of discreteness of tryptophan classes in proteins. Biophys J 2001;81:1710–1734. [PubMed: 11509383]
50. Reshetnyak YK, Koshevnik Y, Burstein EA. Decomposition of protein tryptophan fluorescence spectra into log-normal components. III. Correlation between fluorescence and microenvironment parameters of individual tryptophan residues. Biophys J 2001;81:1735–1758. [PubMed: 11509384]
51. Perez-Rigueiro J, Viney C, Llorca J, Elices M. Mechanical properties of silkworm silk in liquid media. Polymer 2000;41:8433–8439.
52. Bell FI, McEwen IJ, Viney C. Fibre science: supercontraction stress in wet spider dragline. Nature 2002;416:37. [PubMed: 11882884]
53. Karageorgiou V, Meinel L, Hofmann S, Malhotra A, Volloch V, Kaplan D. Bone morphogenetic protein-2 decorated silk fibroin films induce osteogenic differentiation of human bone marrow stromal cells. J Biomed Mater Res A 2004;71:528–537. [PubMed: 15478212]

54. Zoumi A, Yeh A, Tromberg BJ. Imaging cells and extracellular matrix in vivo by using second-harmonic generation and two-photon excited fluorescence. Proc Natl Acad Sci U S A 2002;99:11014–11019. [PubMed: 12177437]

55. Williams RM, Zipfel WR, Webb WW. Interpreting second-harmonic generation images of collagen I fibrils. Biophys J 2005;88:1377–1386. [PubMed: 15533922]

56. Brown E, McKee T, diTomaso E, Pluen A, Seed B, Boucher Y, Jain RK. Dynamic imaging of collagen and its modulation in tumors in vivo using second-harmonic generation. Nat Med 2003;9:796–800. [PubMed: 12754503]

57. Gubler U, Bosshard C. Optical materials: A new twist for nonlinear optics. Nat Mater 2002;1:209–210. [PubMed: 12618776]

58. Foo CWP, Bini E, Huang J, Lee SY, Kaplan DL. Solution behavior of synthetic silk peptides and modified recombinant silk proteins. Applied Physics A-Materials Science & Processing 2006;82:193–203.

59. Lee HS, Teng SW, Chen HC, Lo W, Sun Y, Lin TY, Chiou LL, Jiang CC, Dong CY. Imaging Human Bone Marrow Stem Cell Morphogenesis in Polyglycolic Acid Scaffold by Multiphoton Microscopy. Tissue Eng. 2006

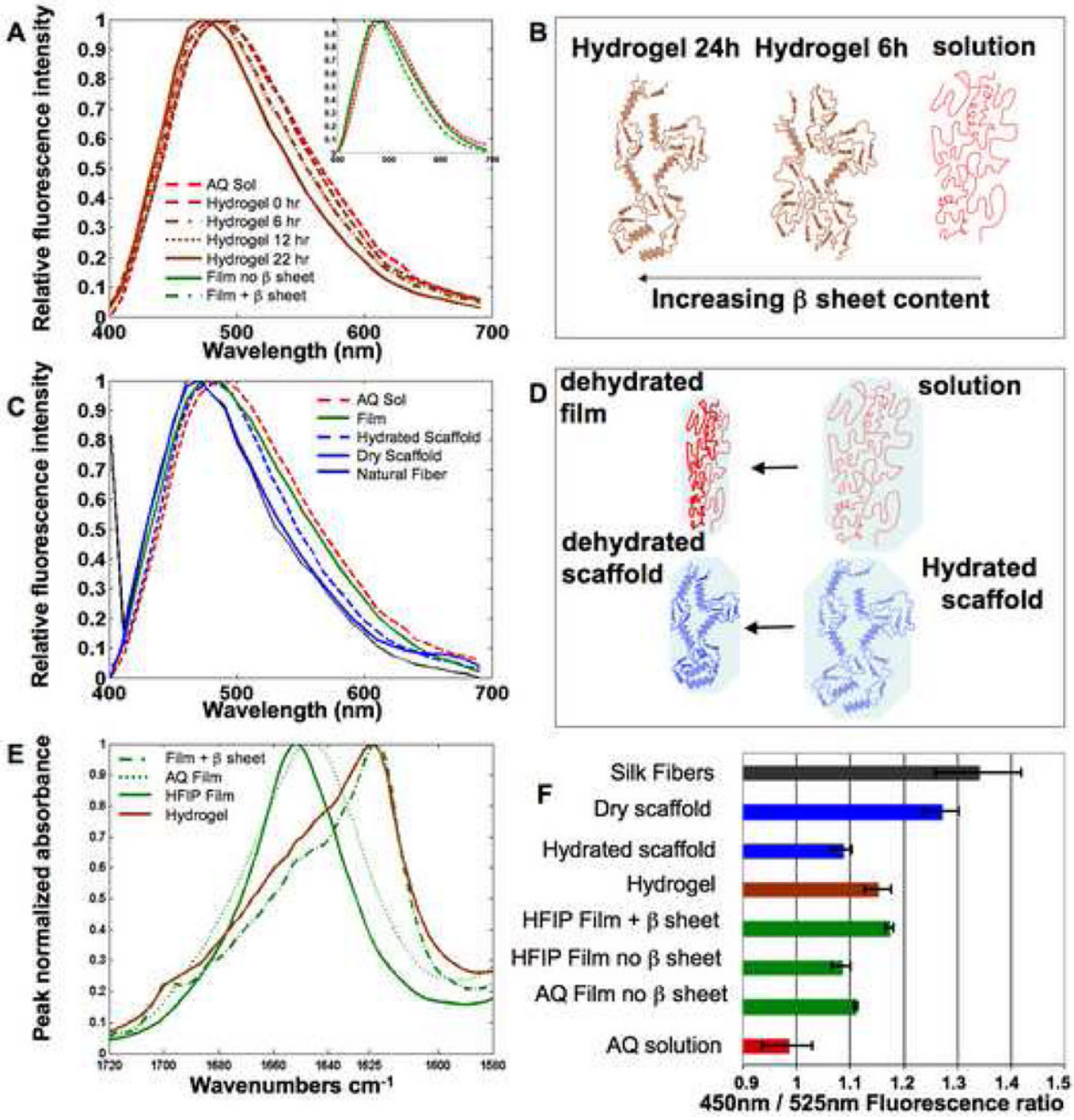

Figure 1. Two photon excited fluorescence spectra of silk biomaterials

The spectral features of TPEF fluorescence resulting from 800 nm excitation of silk biomaterials are sensitive to silk II content and protein hydration. (A) The TPEF spectrum of an aqueous 8% silk solution becomes increasingly blue shifted during gelation induced by addition of HCL. Spectra at 6 and 12 hours of gelation overlap significantly. (A, Inset) A blue shift is also observed in the spectra of HFIP-processed films following b sheet induction by methanol treatment. (B) The main structural changes that are thought to contribute to the observed blue shift in panel (A) are depicted schematically. (C) A blue shift in the TPEF emission spectra is observed with decreased protein hydration. (D) The structural changes that are expected to accompany the level of exposure to a polar water environment are depicted for

the transition from silk solution to silk film and from hydrated to dehydrated scaffold. (E) FTIR spectra reveal β sheet content. (F) Fluorescence intensity ratios of silk biomaterials.

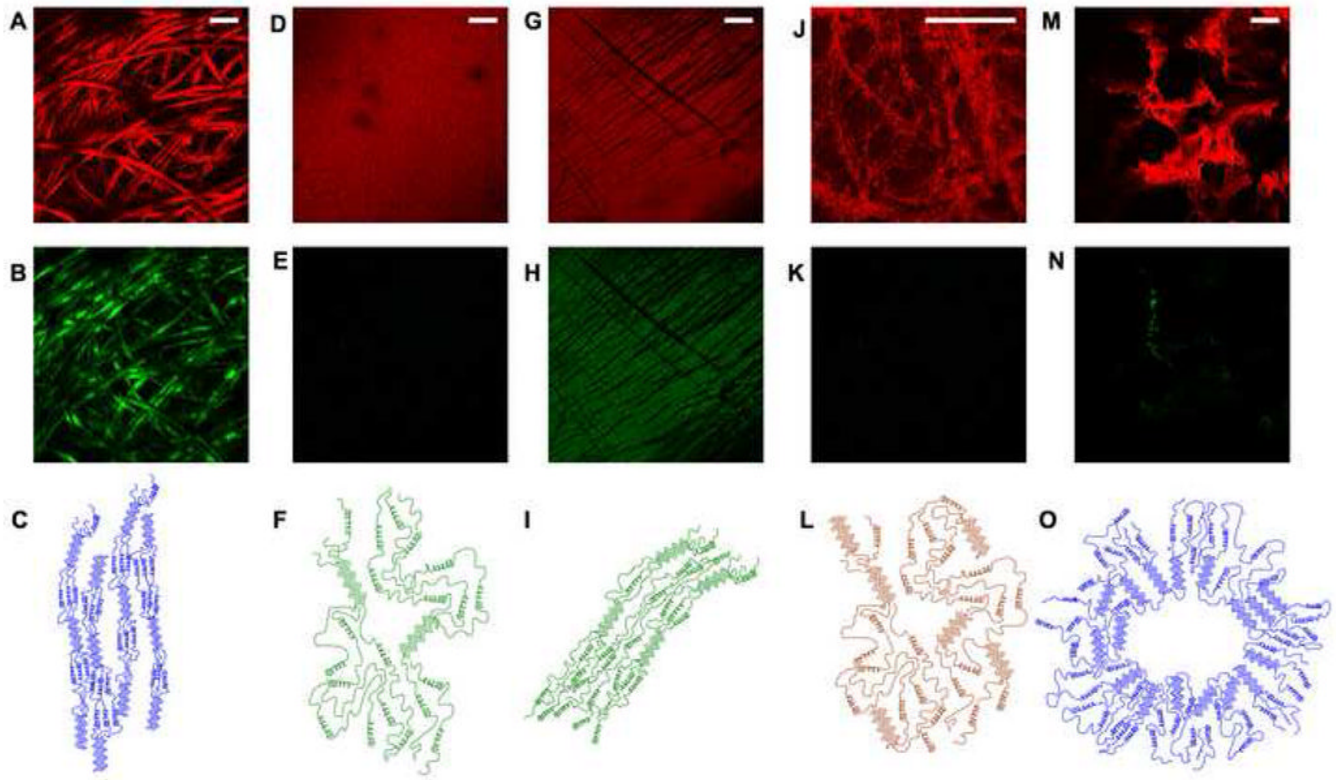

Figure 2. Two photon excited fluorescence and second harmonic generation images of silk biomaterials

Fluorescence (A, D, G, J, M) and SHG (B, E, H, K, N) images collected simultaneously from (A, B) Silk fibers, (D, E) a methanol-treated aqueous film, (G,H) a compressed and stretched methanol-treated aqueous film, (J,K) a hydrogel, and (M,N) a silk scaffold. All images were acquired with 800nm excitation through a 20× (0.7NA) objective. Fluorescence was collected through a 525nm filter with a 25nm band pass. SHG was collected in the forward direction through a 410nm filter with a 20nm band pass. Some of the main secondary structure features, including b sheet content and alignment are depicted for (C) silk fibers, (F) methanol treated films, (I) compressed methanol treated films, (L) hydrogels, and (O) scaffolds. (Bar A-GM =100μm, Bar J = 20μm)

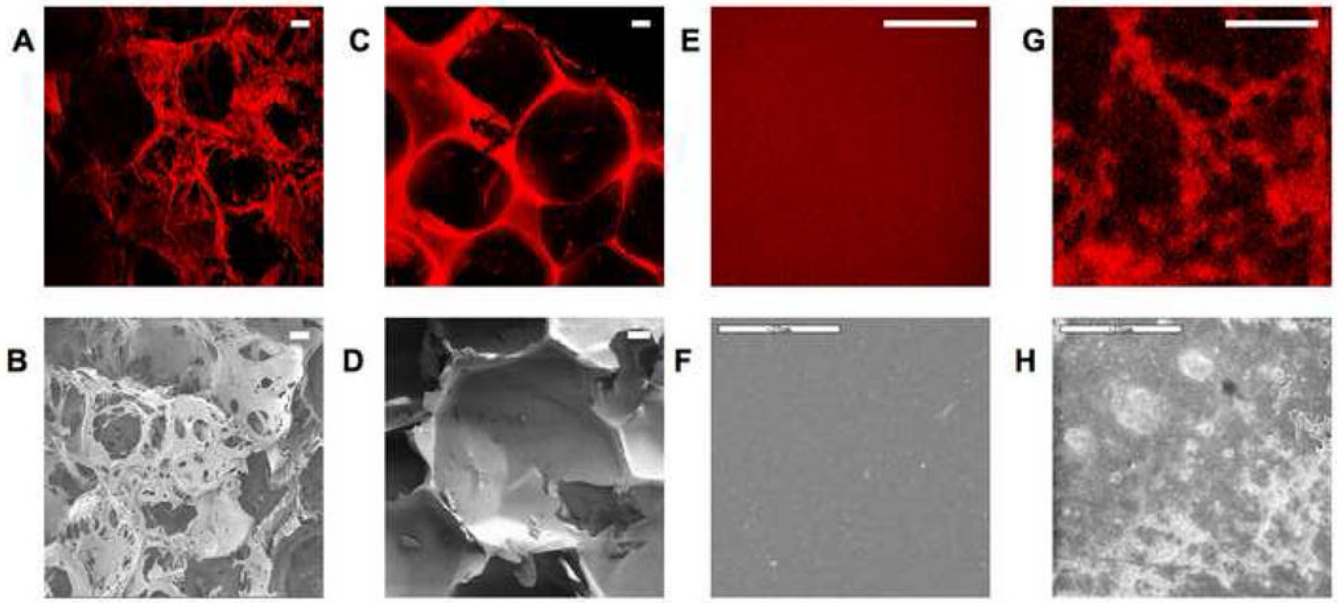

Figure 3. TPEF and SEM images of silk hydrogels and scaffolds

Fluorescence (A,C,E,G) and SEM (B,D,F,H) images reveal comparable morphology in images of (A,B) aqueous silk scaffolds, (C,D) HFIP-processed silk scaffolds (E) 8% silk, 6% HCl. hydrogels and (G), 4% silk, 6% HCl. hydrogels. (Bar A–D =100 μm) (Bar E–H =20 μm)

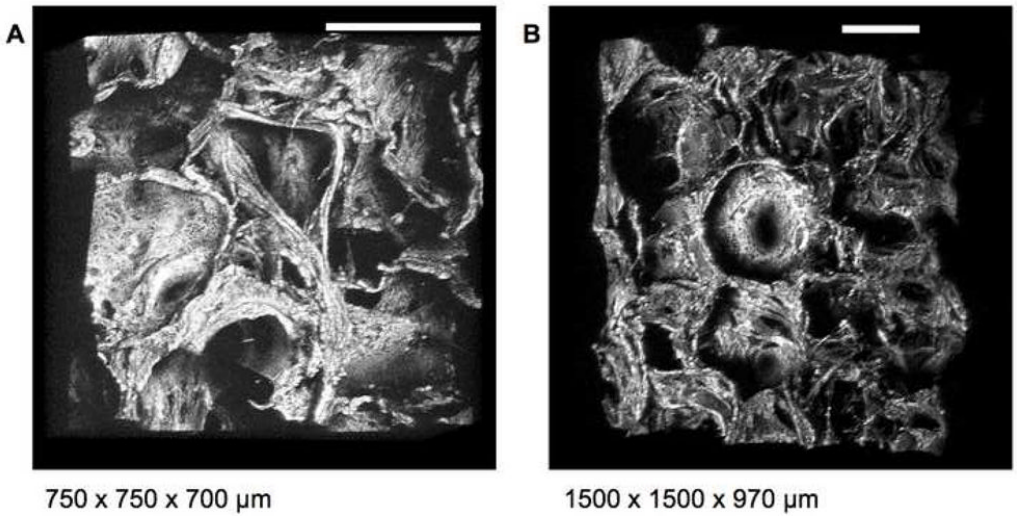

Figure 4. Three dimensional assessment of scaffold morphology

Three dimensional reconstructions of aqueous scaffolds from TPEF optical sections acquired with 800nm excitation using a 455nm bandpass emission filter through an (A) 20× (0.7NA) and (B) 10× (0.3NA) objective allow for observation of scaffold architecture, pore size and interconnections at multiple angles. (Bar = 300 µm) (See corresponding animation Online)

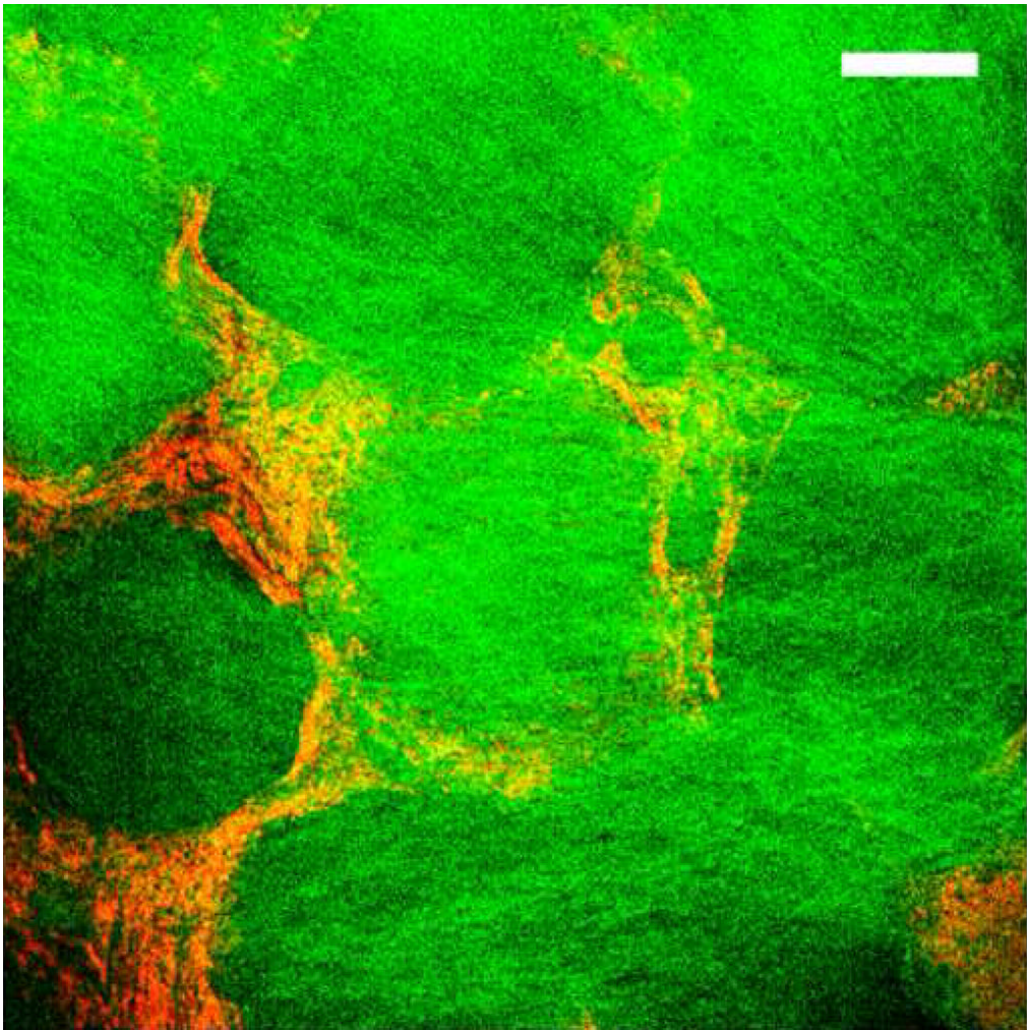

Figure 5. Combined SHG and TPEF imaging

SHG and TPEF images were acquired simultaneously by illuminating an aqueous silk scaffold seeded with collagen producing human mesenchymal stem cells with 800nm. A strong SHG (green) signal from collagen I fibers was collected in the forward direction through a 400nm bandpass filter; TPEF from the silk scaffold (red) was collected through a 455nm bandpass filter. (Bar =100 μm)

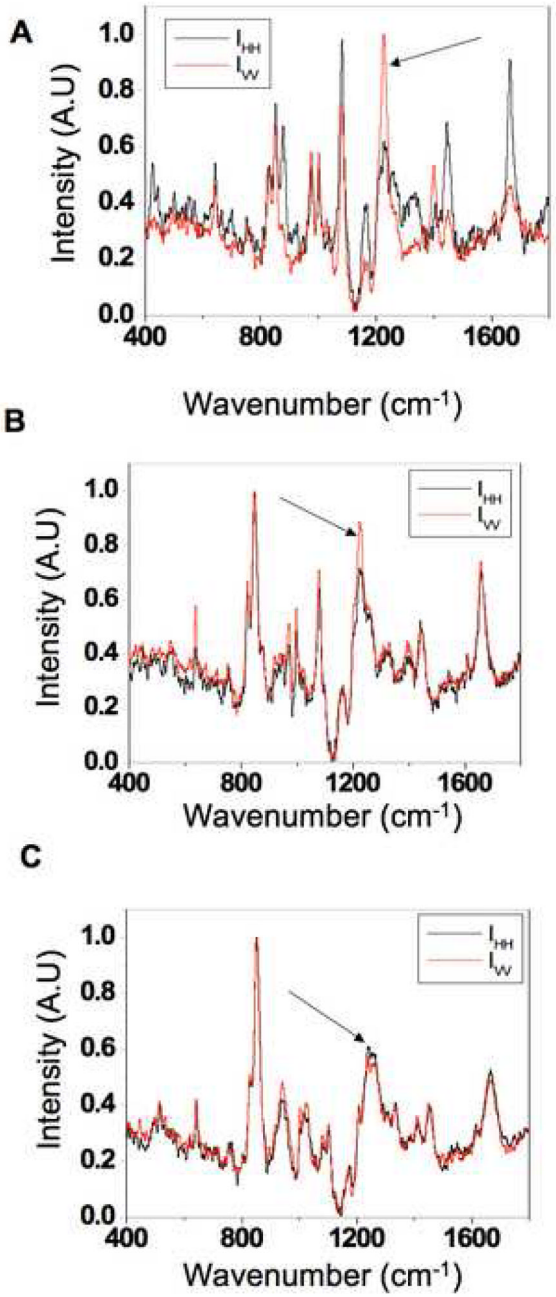

Figure 6. Polarized Raman spectroscopy

Polarization dependent Raman spectra were acquired with copolarized incident and scattered light in either the vertical (red) or horizontal (black) orientation. Polarization dependent spectral features are present in the amide III region (1228 cm^{-1}, arrows) in (A) degummed *B. Mori* cocoon fibers and (B) compressed methanol treated fibroin films indicating Silk II alignment. (C) Uncompressed films with b sheet content showed no polarization dependence in their Raman spectra which infers a random orientation of Silk II.

Table 1

Correlation of silk optical properties with structural and mechanical properties

Material	Morphology	Fibroin tertiary structure	Silk II content	Silk II alignment	Mechanical	Optical	References
Natural Silk Fibers	Filamentous thin	Silk I, Silk II	High (55%)	High	Flexible, high tensile strength	Extreme blue-shifted fluorescence, SHG	[36]
Fibroin Solution	Amorphous	Silk I	None-Low	None	-	Highly red-shifted fluorescence, no SHG	[45]
Fibroin Film	Amorphous, thin	Silk I	None-Low	None	Stiff	Red-shifted Fluorescence, no SHG	[15,43]
Fibroin Film (solvent treated)	Amorphous, thin	Silk I, Silk II	Medium-High (20%)	High with compression	Stiff	Blue-shifted fluorescence, SHG when compressed	[15,43]
Hydrogel	Heterogeneous microstructures, Thick	Silk I, Silk II	Htgn (40–50%)	None	Flexible, weak	Highly blue-shifted fluorescence, no SHG	[45,44]
Scaffold	Porous, Thick	Silk I, Silk II	Medium (22%)	Some	Flexible, strong	Highly blue-shifted fluorescence, SHG along pores	[19,25,40]